

Efficient inversion of 2.5D electrical resistivity data using the discrete adjoint method

Diego Domenzain¹, John Bradford¹, and Jodi Mead²

ABSTRACT

We have developed a memory and operation-count efficient 2.5D inversion algorithm of electrical resistivity (ER) data that can handle fine discretization domains imposed by other geophysical (e.g, ground penetrating radar or seismic) data. Due to numerical stability criteria and available computational memory, joint inversion of different types of geophysical data can impose different grid discretization constraints on the model parameters. Our algorithm enables the ER data sensitivities to be directly joined with other geophysical data without the need of interpolating or coarsening the discretization. We have used the adjoint method directly in the discretized Maxwell's steady state equation to compute the data sensitivity to the conductivity. In doing so, we make no finite-difference approximation on the Jacobian of the data and avoid the need to store large and dense matrices. Rather, we exploit matrix-vector multiplication of sparse matrices and find successful convergence using gradient descent for our inversion routine without having to resort to the Hessian of the objective function. By assuming a 2.5D subsurface, we are able to linearly reduce memory requirements when compared to a 3D gradient descent inversion, and by a power of two when compared to storing a 2D Hessian. Moreover, our method linearly outperforms operation counts when compared with 3D Gauss-Newton conjugate-gradient schemes, which scales cubically in our favor with respect to the thickness of the 3D domain. We physically appraise the domain of the recovered conductivity using a cutoff of the electric current density present in our survey. We evaluate two case studies to assess the validity of our algorithm. First, on a 2.5D synthetic example, and then on field data acquired in a controlled alluvial aquifer, where we were able to match the recovered conductivity to borehole observations.

INTRODUCTION

Electrical resistivity (ER) inversions that take into account the full response of the observed data without assuming subsurface geometry are useful tools for quantitatively characterizing subsurface properties. Moreover, joining ER data with other geophysical methods can achieve higher accuracy on the recovered parameters. For example, Gallardo and Meju (2003) join ER with traveltime seismic data and Doetsch et al. (2010) join ER with traveltime ground-penetrating radar (GPR) data. Both of these methods linearize their respective wave-propagation method. In doing so, the domain discretization is relaxed. Emerging inversion methods that use the full waveform of the data demand finer discretization constraints (Courant et al., 1967). For example, Domenzain et al. (2020a) join ER with GPR data by solving for the full physical response given by Maxwell's equations in 2D space.

Given that the discretization of the ER governing equations do not require fine grid meshes along the entire computational domain, using the second-order optimization methods (Kochenderfer and Wheeler, 2019) is common practice in most ER inversion schemes (Loke and Barker, 1996; Oldenburg and Li, 1999; Günther et al., 2006; Pidlisecky et al., 2007). Although useful on ER data, emerging inversion algorithms that join sensitivities from other time-domain geophysical methods demand either (1) interpolation of the subsurface parameters or (2) having both sensitivities on the same computational grid (Domenzain et al., 2020a).

The benefit of joining time-domain methods (such as GPR or seismic) with ER data is twofold: (1) allowing the low spatial fre-

Manuscript received by the Editor 1 June 2020; revised manuscript received 11 January 2021; published ahead of production 14 February 2021; published online 27 April 2021.

Colorado School of Mines, 1500 Illinois Street, Golden, Colorado 78713-8924, USA. E-mail:diegodomenzain@mines.edu (corresponding author); jbradford@mines.edu.

²Boise State University, 1910 W University Drive, Boise, Idaho 83725, USA. E-mail: jmead@boisestate.edu.

^{© 2021} Society of Exploration Geophysicists. All rights reserved.

E226 Domenzain et al.

quency of the ER conductivity solution to constrain the GPR (or seismic) velocity, and (2) letting the high-spatial-frequency sensitivity of the GPR (or seismic data) enhance the ER resolution. Domenzain et al. (2020b) show that the GPR velocity and ER conductivity recovered parameters can benefit from using structural similarity constraints. They do so by directly joining the full-waveform inversion (FWI) GPR sensitivities with the ER sensitivities. It is worth mentioning that FWI schemes can be computationally demanding in memory and operation count. Moreover, recent fielddata FWI inversions of GPR (Keskinen et al., 2017; Zhou et al., 2020) and elastic-seismic (Groos et al., 2017; Pan et al., 2019) data assume a 2D subsurface geometry. Furthermore, most multioffset GPR surveys also assume a 2D subsurface geometry (Forte and Pipan, 2017). This is due to acquisition and computation costs. Therefore, it is desirable to use efficient ER sensitivity computations when joining ER data to an FWI scheme.

To motivate the usefulness of our 2.5D ER inversion method, we briefly discuss three possible field scenarios for GPR and elasticseismic FWI. Ernst et al. (2007) perform 2D FWI of GPR borehole data on an alluvial aquifer, a setting with the usual electrical parameters found in the subsurface. Their inversion domain is 8 × 20 m, and their slowest velocity is 0.07 m/ns. The number of pixels in their domain is approximately 10⁵. Groos et al. (2017) use 2D elastic-seismic FWI to solve for pressure and S-wave velocities. In their work, they consider S-wave velocities as low as 80 m/s. We consider a 2D domain 200 m in length and 20 m in depth with a central frequency of 80 Hz. In this case, the number of pixels in the domain is 106. Brossier et al. (2009) also perform 2D elastic-seismic FWI on a 20×5 km domain with S-wave velocities as low as 1.2 km/s. Although they perform their inversion in the frequency domain, we consider the time-domain scenario with a central frequency of 20 Hz, which yields 10⁷ pixels in the domain. Figure 1a shows the needed memory for the discussed GPR and elastic-seismic FWI examples in the dashed vertical columns.

a) b) Fixed 2D domain Fixed source-sink pair 10¹⁵ 10³⁰ Exploration 10¹⁰ seismic Operation counts Memory (Gb) Shallow seismic 10⁵ 10⁰ 10² 10³ 10⁶ 10⁸ 10¹ Number of 2D pixels Number of source-sink pairs

Figure 1. Efficiency in the double-precision memory storage and operation count for a range of n_y copies of the 2D xz-domain: $1 \le n_y \le 10^4$. The solid black for both panels denotes our 2.5D method ($n_y = 4$). (a) The memory needed to compute the ER sensitivities as a function of domain size for a single source-sink pair. The dark gray denotes the Hessian of the objective function in 3D space. The light translucent gray denotes the 3D gradient descent using the adjoint method. The dashed lines mark the domain size needed for relevant GPR and seismic surveys. (b) The operation count for the fixed GPR domain size shown in (a). The light translucent gray denotes the 3D gradient descent using the adjoint method. The dark gray denotes the 3D adjoint conjugate-gradient method. The dotted line marks the number of source-sink pairs in our field experiment, of which there are 342.

Second-order optimization methods such as quasi-Newton schemes need to store in memory the Hessian of the objective function. In Figure 1a, we see the amount of double precision memory needed to store the Hessian of the objective function for a range of domain sizes in the dark gray:

3D Hessian memory =
$$(\# \text{ of 2D pixels} \cdot n_v)^2$$
, (1)

where pixels refer to the discretized grid nodes of the computational domain and n_y denotes the number of 2D xz-planes in the y-direction of the 3D discretized domain. Values in Figure 1 are shown for $1 \le n_y \le 10^4$. Although memory requirements for the second-order ER inversion schemes are feasible, incorporating time-domain sensitivities from different geophysical methods can drastically increase the amount of memory.

Loke and Barker (1996) and Pidlisecky et al. (2007) approximate the Jacobian of the ER data with a finite-difference scheme at each grid point. Alternatively, more efficient adjoint methods give direct access to the sensitivity of the data in the entire computational domain.

Ellis and Oldenburg (1994) and Günther et al. (2006) use the adjoint method for directly computing (and storing) the Jacobian of the data. Marescot et al. (2008) use the adjoint method for computing the gradient of the objective function. All approaches use a 3D geometry of the subsurface. The approach of Marescot et al. (2008) for computing the gradient involves storing (1) one 3D electric potential, (2) one 3D forward model matrix, and (3) one 3D adjoint field. Using a rectangular grid, the 3D forward model matrix costs roughly five copies of the domain. In total from (1) to (3), we have 1+5+1=7 copies of the 3D domain. The greatest amount of memory needed is

3D gradient method's memory = # of 2D pixels
$$\cdot n_v \cdot 7$$
. (2)

Figure 1a shows the amount of needed memory for this method with $1 \le n_y \le 10^4$ in translucent light gray.

The adjoint method for computing ER sensitivities can be applied by considering either the continuous objective function (Ellis and Oldenburg, 1994; Günther et al., 2006; Marescot et al., 2008) or the discrete objective function (Tripp et al., 1984; Zhang et al., 1995; Pratt et al., 1998; Ha et al., 2006). Tripp et al. (1984) develop a 2.5D ER inversion using a Gauss-Newton approach. Their method stores the Jacobian of the 2.5D data by numerically integrating a cubic spline interpolation of eight 2D Jacobian matrices. Ha et al. (2006) use the discrete adjoint method similar to Pratt et al. (1998) (in the context of acoustic FWI in the frequency domain) for computing a gradient-descent direction in a 2D ER inversion. However, their method does not account for the 3D variability of the subsurface. Moreover, their method requires a numerical transform the observed data as an apparent electric field and does not account for dissolving boundary conditions in the subsurface.

Ha et al. (2006) count the number of operations for the gradientdescent adjoint method inversion as

3D adjoint gradient count =
$$2 \cdot n_s \cdot (\# \text{ of 2D pixels} \cdot n_y)^3 + 2 \cdot n_s \cdot (\# \text{ of 2D pixels} \cdot n_y)^3$$
, (3)

where n_s denotes the number of source-sink pairs in the survey. The first term counts the computation of the forward model, and the second term counts the computation of the adjoint field. Figure 1b shows this operation count for $1 \le n_y \le 10^4$ in light translucent gray.

Zhang et al. (1995) present a 3D ER inversion that exploits matrix-vector multiplication in a Gauss-Newton conjugate-gradient scheme. Similarly, Newman and Hoversten (2000) compute data sensitivities using the adjoint method for controlled-source electromagnetic data in the frequency domain. Most notably, their method does not need to store nor directly invert the Hessian of the objective function. Rather, their approximation of the Hessian exploits sparse matrix-vector multiplications, and it relies on a conjugate-gradient scheme for computing the model update. This allows their needed memory to be similar to equation 2. However, when the domain and the number of source-sink pairs is large, the conjugate gradient can impose significantly larger computing times when compared with gradient-descent methods. The computation of the Hessian times a vector involves six forward model matrix inversions (without counting the synthetic data and adjoint computations), which at each iteration must be computed approximately 10 times for their conjugategradient scheme to converge. In total, at each iteration their scheme takes

3D adjoint conjugate-gradient count =
$$4 \cdot n_s \cdot (\# \text{ of 2D pixels} \cdot n_y)^3$$

 $+ 6 \cdot 10 \cdot 2 \cdot n_s \cdot (\# \text{ of 2D pixels} \cdot n_y)^3$, (4)

where the first term corresponds to computing the gradient and the second term corresponds to computing the model update using conjugate gradient. Figure 1b shows this operation count for $1 \le n_v \le$ 10⁴ in dark gray.

For our ER adjoint method inversion, we adapt the acoustic FWI of Pratt et al. (1998) to a 2D ER inversion that does not need to transform the observed data into an apparent electric field (Ellis and Oldenburg, 1994; Zhang et al., 1995; Domenzain et al., 2020a). Using the approximation of Pidlisecky and Knight (2008), we approximate the 3D subsurface with a linear combination of 2D electric potentials for a 2.5D solution. This linear combination in the continuous case is the inverse Fourier transform in the k_y domain of the 3D solution, which is the physically accurate 2.5D solution. We then use this 2.5D electric potential approximation to compute the 2.5D conductivity sensitivity as a linear combination of the 2D sensitivities. We use a gradient-descent algorithm that relieves the need to store the Jacobian of the data (by exploiting sparse matrix-vector multiplication) or to approximate the Hessian of the objective function. Furthermore, assuming a 2.5D subsurface enables us to further reduce memory requirements compared with 3D adjoint methods using the gradient descent (Marescot et al., 2008). For our 2D forward model, we use dissolving boundary conditions in the subsurface (Dey and Morrison, 1979), which relaxes the need to do extra padding of the domain.

At most, the amount of memory for computing the 2.5D ER sensitivities with our method is given by the memory needed to store (1) the 2D electric potentials, (2) one 2D adjoint field, and (3) one 2D forward model matrix. We use four 2D electric potentials as do Pidlisecky and Knight (2008). Using a rectangular grid discretization, each forward model matrix costs roughly five copies of the domain. In total, from (1) to (3), we have 4 + 1 + 5 = 10 copies of the domain:

Our 2.5D method's memory =
$$\#$$
 of 2D pixels \cdot 10. (5)

Figure 1a shows the amount of memory needed with our method for a range in domain size in black. Our use of the adjoint method and the 2.5D approximation exponentially outperforms memory requirements for the 2D and 3D Hessian. Compared to storing the 2D Jacobian of the data (of size number of pixels × number of data points), our algorithm costs significantly less memory when the number of data points is larger than 10. Moreover, a linear reduction in memory is achieved when compared to the 3D gradient adjoint method. In this case, the amount of memory gained is $n_v \cdot 7/10$.

We use a similar version of equation 3 to count the operations needed in our method. However, we use $n_v = 1$ because our computations are only in the 2D domain. We then multiply for the four copies of our 2D domain, which are needed to approximate the 2.5D subsurface:

Table 1. Double-precision memory in units of gigabytes needed for the ER sensitivities on the domains given by the GPR and seismic surveys depicted in Figure 1a.

Method	Domain size			
	GPR	Shallow seismic	Exploration seismic	
3D Hessian	8×10^{9}	8×10^{11}	8×10^{13}	
2D Hessian	8 × 10	8×10^{3}	8×10^{5}	
3D adjoint gradient descent	5×10	5×10^{2}	5×10^{3}	
2.5D adjoint gradient descent	8×10^{-3}	8×10^{-2}	8×10^{-1}	
2D adjoint gradient descent	5×10^{-3}	5×10^{-2}	5×10^{-1}	

Bold font denotes the values found by our method described in the manuscript.

The values for the 3D Hessian and 3D adjoint gradient descent were taken with $n_v = 10^4$.

E228 Domenzain et al.

our 2.5D method's count =
$$16 \cdot (\# \text{ of } 2D \text{ pixels})^3$$
. (6)

Figure 1b shows our method's operation count in solid black. We note a linear reduction in operation count by a factor of n_v^3 for the 3D adjoint conjugate gradient and the 3D adjoint gradient methods.

In Table 1, we show specific values of how much memory is needed for each relevant field data example considered and for each method in Figure 1a. Assuming a 2.5D subsurface geometry, an increase of less than an order of magnitude from the best 2D scenario gives a more accurate physical model with our 2.5D method. Conversely, up to four orders of magnitude can be gained with our method when compared with the least memory-consuming 3D method. In Table 2, we show the operation counts taken from Figure 1b along the dotted line, which marks the fixed number of source-sink pairs that we used in our field data example. We again note a benefit for using our 2.5D method. In this case, the cost increase compared with 2D is still less than an order of magnitude, whereas the cost increase from using a 3D method is more than one order of magnitude in the operation count.

Given the low memory storage and modest operation count, our algorithm can be used for joint inversion with data whose forward models impose finer grid constraints without the need to interpolate the parameters. Furthermore, our algorithm accomplishes this task with less computation cost than using a 3D method.

We assess the accuracy of the recovered conductivity at depth using a measure of electric current density in our survey throughout all iterations. Our method relies on the physical principle that the sensitivity of surface-acquired ER data is given by electric current lines that return to the surface. Although other methods exist (Oldenburg and Li, 1999) and have been successful in field surveys (Oldenborger et al., 2007b), they are costly to compute because more than one inversion is needed for their construction. However, the (costly) exploration of the parameter space given by multiple inversions of the data give a reliable region for appraising the solution. Rather than presenting a substitute for existing methods, we present ours as a computationally cheap alternative that takes into account the physics of the ER survey and the different sensitivities of the data throughout the inversion. We show that, at worst, our approach is conservative in appraising the solution domain.

We show the usefulness of our work with a synthetic example and field data acquired at an alluvial aquifer near Boise, Idaho, USA.

Table 2. Operation count needed for computing ER sensitivities on the domain given by the GPR survey depicted in Figure 1b.

	Operation count
3D adjoint conjugate gradient	5×10^{31}
3D adjoint gradient descent	1×10^{30}
2D adjoint conjugate gradient	5×10^{19}
2.5D adjoint gradient descent	5×10^{18}
2D adjoint gradient descent	1×10^{18}

Bold font denotes the values found by our method described in the manuscript

The number of source-receiver pairs is taken from our field data example, of which there are 342. The values for the 3D adjoint conjugate-gradient scheme and 3D adjoint gradient descent were taken with $n_v = 10^4$.

Both experiments consist of only surface-acquired ER data. We perform our inversions on finely discretized grids in which each pixel is square and has a side length equal to 0.05 m. These discretization values comply with numerical stability criteria for a GPR 2D FWI on commonly encountered scenarios. For example, Ernst et al. (2007) use a 0.14 m spacing for their inversion and 0.04 m for their forward modeling on the same alluvial aquifer. Furthermore, the physical size of our entire domain for the ER field data inversion is also relevant for GPR exploration (15 m in depth and 45 m across). This enables our algorithm to potentially join ER and GPR sensitivities of the subsurface without the need for interpolating their respective domains. We compare our results with previous borehole low-frequency conductivity studies at the same site (Oldenborger et al., 2007a; Mwenifumbo et al., 2009) and find similar results for the petrophysical parameters and conductivity values.

Finally, we compare our finely recovered conductivity with that of the commercially available software Res2DInv (Loke, 2006) on the smallest possible horizontal grid size allowed by the software. Although both conductivities exhibit similar features, our algorithm is capable of handling grid sizes of at least an order of magnitude smaller.

METHODS

ER 2D forward model

Assuming Ohm's law, the 2D physics of the ER experiment are given by the steady-state Maxwell's equations (Pidlisecky et al., 2007):

$$-\nabla \cdot \sigma(x,z)\nabla \varphi(x,z) = \underbrace{i(\delta(x-s_{+}) - \delta(x-s_{-}))}_{s(x,z)}, \quad (7)$$

where φ is the electric potential, i is the current intensity, s_+ is the source-sink location, and σ is the electrical conductivity. Because we are assuming a 1D survey line perpendicular to the y-axis, the

ER 2.5D forward model

- 1. retrieve from memory (or compute) k and ω ,
- 2. choose $k_i \in \mathbf{k}$ and
- 3. build $\mathbf{L}_i = \mathbf{L}^i + k_i^2 \, \boldsymbol{\sigma}$ with the right boundary conditions for that k_i ,
- 4. solve $\mathbf{L}_i \tilde{\boldsymbol{\varphi}}_i = \frac{\mathbf{s}}{2}$ for $\tilde{\boldsymbol{\varphi}}_i$ and store,
- 5. repeat 2-4 until all $k_i \in \mathbf{k}$ have been used,
- 6. compute φ , d and e,

$$\varphi = \frac{2}{\pi} \sum_{i} \omega_{i} \tilde{\varphi}_{i}$$
$$\mathbf{d} = \mathbf{M} \varphi$$
$$\mathbf{e} = \mathbf{d} - \mathbf{d}^{o}$$

Figure 2. Algorithm for computing the 2.5D electric potential given a source s and conductivity σ .

source term s does not depend on y. Moreover, because we are considering source-sink locations only at the surface (z = 0), the source and sink locations $(s_+ \text{ and } s_-)$ only depend on x.

We discretize equation 7 using a finite-volume method with the Neumann and Robin boundary conditions at the air-ground interface and in the subsurface, respectively. The discretization is adapted from Dey and Morrison (1979) for our 2D case. We express our discretization as a matrix-vector product,

$$\mathbf{L}\boldsymbol{\varphi}_{2D} = \mathbf{s},$$

$$\mathbf{d}_{2D} = \mathbf{M}\boldsymbol{\varphi}_{2D},$$
(8)

where L is the discretized differential operator of equation 7, φ_{2D} is the 2D electric potential, s is the source term, M is the measuring operator that computes observed voltages, and \mathbf{d}_{2D} is the data of the experiment for one source-sink location. For every pixel in the domain, the matrix L has as many nonzero entries as neighbors and another entry for itself. Because an inner pixel has four neighbors, an upper bound for the nonzero bands of L is five, with each band having as many elements as pixels that are in the domain.

Inversion of 2D ER data

In this section, we follow Domenzain et al. (2020a) and briefly review the 2D discrete adjoint method. In the "Inversion of 2.5D ER data" section, we will generalize this method for our 2.5D solution. We optimize the objective function

$$\Theta_{2D}(\sigma; \mathbf{d}_{2D}^{o}) = \left\| \underbrace{\mathbf{d}_{2D} - \mathbf{d}_{2D}^{o}}_{\mathbf{e}_{2D}} \right\|_{2}^{2}, \tag{9}$$

with respect to the conductivity, where \mathbf{e}_{2D} is the residual of the data in the 2D space. Domenzain et al. (2020a) show that the gradient \mathbf{g}_{2D} of the objective function Θ_{2D} with respect to σ for one source can be expressed as

ER 2.5D objective function gradient

- 1. compute the 2.5D forward model to get all $\tilde{\varphi}_i$ and e,
- 2. choose $k_i \in \mathbf{k}$,
- 3. build L_i and solve for $\tilde{\mathbf{v}}_i$,

$$\mathbf{L}_i = \mathbf{L}^i + k_i^2 \, \mathbf{\sigma},$$
$$\mathbf{L}_i^{\top} \tilde{\mathbf{v}}_i = \mathbf{M}^{\top} \mathbf{e},$$

4. build S_i and compute \tilde{g}_i ,

$$\begin{split} \mathbf{S}_i &= -\left((\nabla_{\sigma}\mathbf{L}^i)\tilde{\mathbf{\varphi}}_i\right)^{\top} - k_i^2 \; \mathsf{diag}(\tilde{\mathbf{\varphi}}_i)^{\top}, \\ \tilde{\mathbf{g}}_i &= \mathbf{S}_i\tilde{\mathbf{v}}_i \end{split}$$

- 5. repeat 2-4 until all k has been used,
- 6. $\mathbf{g} = \frac{2}{\pi} \sum_{i} \omega_i \, \tilde{\mathbf{g}}_i$.

Figure 3. Algorithm for finding the 2.5D gradient g.

$$\mathbf{L}^{\mathsf{T}}\mathbf{v}_{2\mathsf{D}} = \mathbf{M}^{\mathsf{T}}\mathbf{e}_{2\mathsf{D}},$$

$$\mathbf{g}_{2\mathsf{D}} = \mathbf{S}\mathbf{v}_{2\mathsf{D}},$$
 (10)

where

$$\mathbf{S} = -((\nabla_{\sigma} \mathbf{L}) \boldsymbol{\varphi}_{2D})^{\mathsf{T}} \tag{11}$$

is a sparse banded matrix whose entries are explicitly calculated. Equations 10 and 11 can also be expressed as

$$\mathbf{g}_{\mathrm{2D}} = \mathbf{J}_{\mathrm{2D}}^{\mathsf{T}} \mathbf{e}_{\mathrm{2D}},$$

$$\mathbf{J}_{\mathrm{2D}} = \mathbf{M} \mathbf{L}^{-1} \mathbf{S}^{\mathsf{T}}.$$
 (12)

We note that, because we are computing the derivative with respect to σ on the discrete operator L, the boundary conditions of L are also taken into account in S. The number of nonzero entries in S is the same as L. Each column of S accounts for one virtual source (Pratt et al., 1998; Ha et al., 2006), and in a given iteration it is computed once per source s.

ER 2.5D forward model

Equation 7 disregards the 3D nature of the earth that is present in field data. To account for 3D structure while still assuming no significant change in the y-direction, we can express the governing physics of the ER experiment as

$$-\nabla \cdot \sigma(x, z) \nabla \varphi(x, y, z) = s(x, z). \tag{13}$$

To solve equation 13, we use the Fourier-cosine transform in the k_y domain (Pidlisecky and Knight, 2008),

$$-\nabla \cdot \sigma \nabla \tilde{\varphi}(x, k_y, z) + k_y^2 \sigma \tilde{\varphi}(x, k_y, z) = \frac{1}{2} s(x, z), \quad (14)$$

and then we use the inverse Fourier-cosine transform to get the electric potential solution in the xz-plane,

$$\varphi(x, y = 0, z) = \frac{2}{\pi} \int_0^\infty \tilde{\varphi} dk_y.$$
 (15)

As explained by Pidlisecky and Knight (2008), discretizing equation 15 amounts to optimizing for an array **k** of k_y values and a corresponding array ω of weights ω . For completeness, we include the details of this optimization in Appendix A. The terms **k** and ω do not depend on the subsurface conductivity. They only depend on the source-receiver geometry.

Once k and ω have been computed, we discretize equation 14 for each weight k_i in **k** as

$$\mathbf{L}_i = \mathbf{L}^i + k_i^2 \mathbf{\sigma},\tag{16}$$

where L^i is very similar as in equation 8 but the Robin boundary conditions in the subsurface are now different, as dictated in equation A-2. The ith 2D forward model is

$$\mathbf{L}_{i}\tilde{\boldsymbol{\varphi}}_{i} = \frac{\mathbf{s}}{2},$$

$$\tilde{\mathbf{d}}_{i} = \mathbf{M}\tilde{\boldsymbol{\varphi}}_{i}.$$
(17)

E230 Domenzain et al.

The full 2.5D forward model, i.e., the discretized expression of equation 15, is

$$\boldsymbol{\varphi} = \frac{2}{\pi} \sum_{i} \tilde{\boldsymbol{\varphi}}_{i} \omega_{i}. \tag{18}$$

In Figure 2, we give all of the steps of the algorithm for computing φ .

Inversion of 2.5D ER data

Now that we have formulated the 2D gradient computation (see equation 10) and the 2.5D forward model (see equations 17 and 18), we explain how to compute the 2.5D gradients for a 2.5D conductivity solution. We now want to optimize the objective function,

$$\Theta(\mathbf{\sigma}; \mathbf{d}^o) = \left\| \mathbf{d} - \mathbf{d}^o \right\|_2^2, \tag{19}$$

with respect to the conductivity where e is the residual of the data in 2.5D space. We compute the gradient g of Θ by

$$\mathbf{g} = \mathbf{J}^{\mathsf{T}} \mathbf{e},\tag{20}$$

where $\mathbf{J} = \nabla_{\sigma} \mathbf{d}$. The gradient operator ∇_{σ} is a row vector with the ith entry being the partial derivative ∂_{σ_i} . To find an expression for \mathbf{J} , we first write \mathbf{d} in terms of $\tilde{\mathbf{d}}_i$,

$$\mathbf{d} = \mathbf{M}\boldsymbol{\varphi} = \mathbf{M} \underbrace{\frac{2}{\pi} \sum_{i} \omega_{i} \tilde{\boldsymbol{\varphi}}_{i}}_{\boldsymbol{\varphi}}, = \frac{2}{\pi} \sum_{i} \omega_{i} \underbrace{\mathbf{M} \tilde{\boldsymbol{\varphi}}_{i}}_{\tilde{\mathbf{d}}_{i}} = \frac{2}{\pi} \sum_{i} \omega_{i} \tilde{\mathbf{d}}_{i}.$$
(21)

We can now apply ∇_{σ} to equation 21,

$$\nabla_{\sigma} \mathbf{d} = \frac{2}{\pi} \sum_{i} \omega_{i} \underbrace{\nabla_{\sigma} \tilde{\mathbf{d}}_{i}}_{\mathbf{J}_{i}} = \underbrace{\frac{2}{\pi} \sum_{i} \omega_{i} \mathbf{J}_{i}}_{\mathbf{J}_{i}}.$$
 (22)

Equation 22 is a method for computing **J**. By substituting equation 22 into equation 20, we have

$$\mathbf{g} = \frac{2}{\pi} \left(\sum_{i} \omega_{i} \mathbf{J}_{i} \right)^{\mathsf{T}} \mathbf{e}$$

$$= \frac{2}{\pi} \sum_{i} \omega_{i} \mathbf{J}_{i}^{\mathsf{T}} \mathbf{e}.$$
(23)

In the last equality, we write $\tilde{\mathbf{g}}_i = \mathbf{J}_i^{\mathsf{T}} \mathbf{e}$, because with a similar approach as equation 10, from equation 17 we have

$$\mathbf{L}_{i}^{\mathsf{T}}\tilde{\mathbf{v}}_{i} = \mathbf{M}^{\mathsf{T}}\mathbf{e},$$

$$\tilde{\mathbf{g}}_{i} = \mathbf{S}_{i}\tilde{\mathbf{v}}_{i},$$
(24)

where

$$\mathbf{S}_{i} = -((\nabla_{\sigma} \mathbf{L}^{i}) \tilde{\boldsymbol{\varphi}}_{i})^{\mathsf{T}} - k_{i}^{2} \operatorname{diag}(\tilde{\boldsymbol{\varphi}}_{i})^{\mathsf{T}}, \tag{25}$$

and similar to equation 12, we have $\mathbf{J}_i = \mathbf{M} \mathbf{L}_i^{-1} \mathbf{S}_i^{\mathsf{T}}$. In conclusion, we compute the gradient \mathbf{g} of equation 19 by

$$\mathbf{g} = \frac{2}{\pi} \sum_{i} \omega_i \tilde{\mathbf{g}}_i. \tag{26}$$

Figure 3 gives a summary for computing g.

Updating the conductivity

Equation 26 gives the gradient \mathbf{g} for equation 19 with respect to $\boldsymbol{\sigma}$ for one source. We regularize \mathbf{g} by adding the normalized residual of a reference conductivity $.\boldsymbol{\sigma}_o$ and then smoothing in the space-frequency domain. After computing \mathbf{g} with equation 26 and normalizing by its largest magnitude, we have

$$\mathbf{g} \leftarrow \mathbf{g} + \beta \frac{\mathbf{\sigma} - \mathbf{\sigma}_o}{\max(abs(\mathbf{\sigma} - \mathbf{\sigma}_o))}, \tag{27}$$

where β is a fixed number smaller than one. The gradient ${\bf g}$ exhibits large values near the receiver locations. To suppress these artifacts, we smooth ${\bf g}$ using a space-frequency low-pass filter (Taillandier et al., 2009; Groos et al., 2017; Domenzain et al., 2020a). In practice, we use a Gaussian of width λ ,

$$\lambda = \frac{1}{\Delta r \cdot a},\tag{28}$$

where Δr is the minimum electrode spacing in meters and a is close to one, loosely $0.5 \le a \le 1.5$. Although similar to the conventional spatial-derivative matrix used for smoothing data sensitivities, this approach proves more effective in removing receiver artifacts when using the adjoint method. As with any smoothing or regularization operator, a compromise is made between the spatial resolution of the solution and the resulting fit to the data. Ideally, a filter of width $1/\Delta r$ should suffice. However, as with any regularization parameter, λ depends on the true subsurface parameters and the initial conductivity model. Therefore, a fixed value of λ ranging more and less than $1/\Delta r$ has to be found for each specific case.

To enforce positivity constraints on σ , we do a logarithmic change of variable on the objective function $\Theta(\sigma) = \Theta(\ln(\sigma))$ (Meles et al., 2010). Using the chain rule, we have

$$\mathbf{g}_{\sigma} = \frac{1}{\sigma} \odot \mathbf{g}_{\ln \sigma}, \tag{29}$$

where the subscript denotes the variable under consideration and \odot denotes the element-wise multiplication. Computing the update, using equation 29 and taking the inverse of the logarithm, we have

$$\ln(\mathbf{\sigma}_{i+1}) = \ln(\mathbf{\sigma}_i) - \alpha \mathbf{g}_{\ln \mathbf{\sigma}},$$

$$\mathbf{\sigma}_{i+1} = \mathbf{\sigma}_i \odot \exp(-\alpha \cdot \mathbf{\sigma}_i \odot \mathbf{g}_{\mathbf{\sigma}}).$$
 (30)

Equation 30 holds true for one source-sink location. In practice, however, we update σ once all update directions $-\alpha \mathbf{g}$ for all sources in our survey have been computed. The step size α is found as proposed by Pica et al. (1990) and adapted for our ER inversion by Domenzain et al. (2020a). This step-size computation also constrains the range of possible values for σ by an arbitrary user-defined interval. In practice, we define this interval by the minimum

and maximum values of the observed apparent resistivities. The entire process of computing the step-size only costs one 2.5D forward model computation.

The global update $\Delta \sigma$ is the average of all update directions over all source-sink pairs. At late iterations when the sensitivity of our data is weak, $\Delta \sigma$ might struggle to find a true descent direction. This issue can be addressed by using momentum (Rumelhart et al., 1986), which only costs the storage of the previous iteration update, $\Delta \sigma$. The final update for the conductivity is given by

$$\Delta \mathbf{\sigma} \leftarrow \Delta \mathbf{\sigma} + \beta_{\bullet} \Delta \mathbf{\sigma}_{\bullet},$$

$$\mathbf{\sigma} \leftarrow \mathbf{\sigma} \odot \exp(\mathbf{\sigma} \odot \Delta \mathbf{\sigma}),$$
 (31)

where β_{\bullet} is a fixed number smaller than one. Figure 4 shows the full algorithm for our inversion.

Solution appraisal

Physically, the sensitivity at the depth of the ER survey is related to the electric current density of all source-sink pairs in the survey.

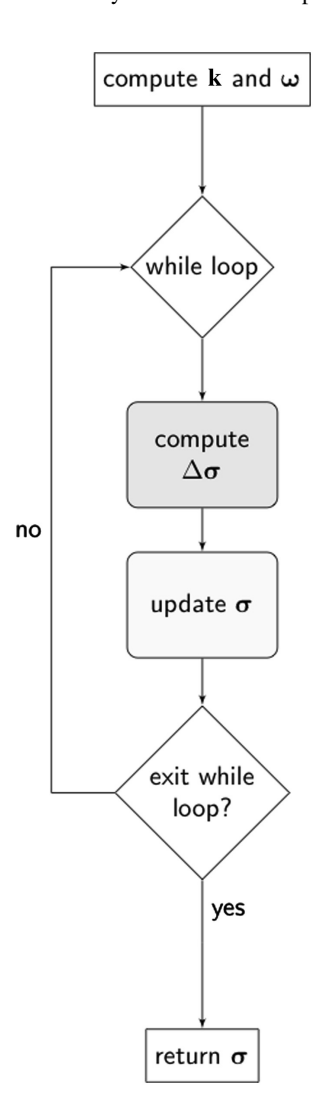


Figure 4. The 2.5D inversion algorithm.

Depending on our initial model, each forward model in the ER inversion might have different electric current densities throughout iterations. Therefore, throughout the inversion, the illumination of the subsurface changes as a function of the observed data and the initial conductivity model.

At each iteration i, we quantify the total electric current density in our inversion by summing the absolute value of the electric potentials φ given by our forward models (see equation 18),

$$\Psi_i = \sum_j |\boldsymbol{\varphi}_j|,\tag{32}$$

where j runs through all forward models. As iterations proceed, we keep adding the previous Ψ_i to the new one to obtain a final measure of electric current density Ψ , then we normalize Ψ by its largest amplitude,

$$\Psi = \sum_{i} \Psi_{i}$$

$$\Psi \leftarrow \frac{\Psi}{\max(\Psi)}.$$
(33)

Given the harmonic nature of the electric potential, the field Ψ will have a level curve beyond which the electric current lines will no longer return to the surface. We choose this level curve as a cutoff for Ψ from which all level curves below this cutoff are considered to not contain relevant information. The resulting image for Ψ is then a collection of ones in the xz-plane above the cutoff value.

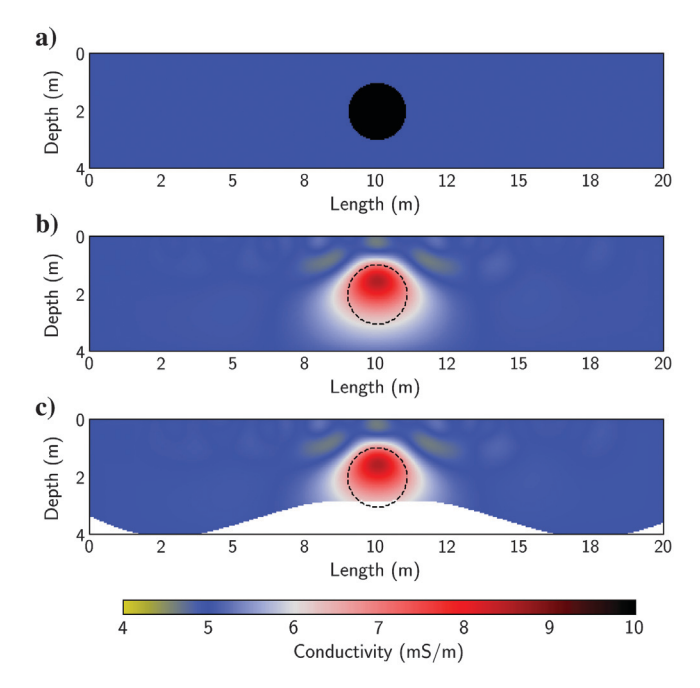


Figure 5. (a) True, (b) recovered, and (c) appraised conductivity for the synthetic example. The dashed cyan line represents a borehole location. The dashed black line represents the contour of the cylinder. The pixel size is 0.05 m on each side.

EXAMPLES

In this section, we verify the validity of our algorithm on two scenarios: a synthetic 2.5D example and on field data aguired in a controlled alluvial aquifer.

Synthetic data example

We test our algorithm on a synthetic scenario as shown in Figure 5a. The model consists of a 20×4 m subsurface domain with a 10 mS/m cylindrical anomaly embedded in a 5 mS/m background. We use 17 electrodes spaced 1 m apart with all possible dipoledipole, Wenner, and Schlumberger arrays. The full discretized domain is of size 81×401 with a square pixel size of 0.05 m.

Our initial model is a homogeneous conductivity equal to the background of our model. Besides smoothing the gradients g,

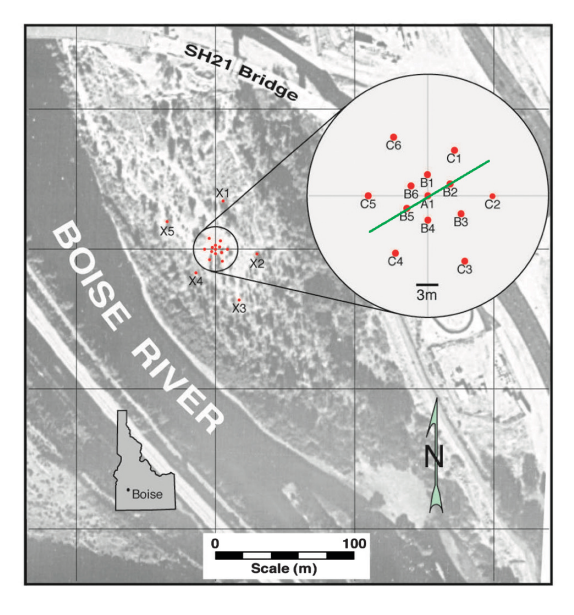


Figure 6. Geographic location of the BHRS. The red dots denote the existing boreholes. Our survey line crossed boreholes B5, A1, and B2 as shown by the green line.

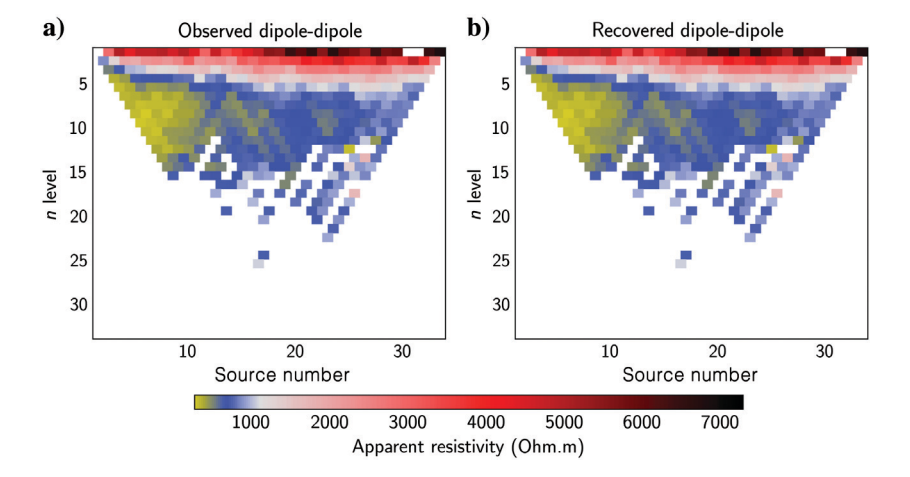


Figure 7. Dipole-dipole pseudosection with a-spacing equal to 1 m from the BHRS.

for this example, we do not impose regularization on the inversion. We choose a smoothing factor of a = 1.1 (see equation 28) and a value of $\beta = 0.02$.

In Figure 5b, we see the recovered conductivity in the entire computational domain, and in Figure 5c, we see the recovered conductivity with a current density cutoff of 0.025% of the maximum value of Ψ (see equation 33). Our solution-appraisal technique is able to remove parts of the domain in which we have a poor constraint in our solution (the bottom of the domain) but keep parts of the domain in which the recovered conductivity remains close to the true model. We note that by choosing a cutoff that eliminates the electric current leaving the domain, we are conservatively assessing our solution.

Field data example

We acquired field data at the Boise Hydrological Research Site (BHRS) in May 2019. The site is an alluvial aguifer next to the Boise river as shown in Figure 6 (modified from Barrash et al., 1999). The water flow in the river is controlled by a nearby dam and is increased throughout spring as warmer temperatures thaw the snowpack in the nearby Sawtooth Mountain Range (Barrash et al., 1999). We planned for our experiment to take place when the water table was at its highest point without the site being flooded. This choice was made to increase the electric current of our survey past the water table boundary and improve our depth sensitivity. We used an IRIS Syscal Pro resistivity system with a total of 36 electrodes spaced 1 m apart in a 1D line perpendicular to the river as shown in Figure 6. Our survey consisted of all possible dipole-dipole and Wenner arrays for a total of 1175 sourcereceiver pairs. Although approximately planar, the ground surface dips slightly (0.4 m over 36 m) toward the river.

Based on the knowledge of site stratigraphy (e.g., Bradford et al., 2009), the position of the line perpendicular to the river was chosen to enhance the variability of conductivity in the xz-plane while keeping the y-coordinate variability of the conductivity approximately constant. For each source-receiver pair, the raw data recorded by the Syscal Pro are in units of volts, paired with readings of source current magnitude (positive and in units of amperes), apparent resistivites computed by the system (in units of ohms per meter), and a measure of standard deviation (each source was performed eight times).

Preprocessing

For our inversion, we use only the voltage readings. However, before performing our inversion, we use all of the Syscal Pro data to enhance the quality of our inversion in three steps. (1) Remove the negative apparent resistivities given by the Syscal Pro system because these data points are not physical and are contaminated by noise. (2) Eliminate data points whose standard deviation is more than a fixed cutoff. In this case, the cutoff was five standard deviations. (3) Divide the voltage readings by their respective source current magnitude. This last step is done to enable multi-source-receiver pairs in each forward model of our inversion. Our data consist of 342 different source-sink positions and a total of 1175 data points. The next step is to compute the weights **k** and ω (see Figure A-1). Figures 7a and 8a show the observed but preprocessed apparent resistivities of the dipole-dipole with a-spacing equal to 1 m and Wenner arrays, respectively.

Inversion

Our initial model is a homogeneous subsurface with conductivity

equal to 2 mS/m. We regularize the inversion using a homogeneous reference conductivity equal to our initial model and weighting factors of $\beta =$ 0.001 and $\beta = 0.5$. The full discretized domain is of size 301×901 with a square pixel size of 0.05 m, i.e., 15 m deep and 45 m across. Figure 9 shows the recovered conductivity corrected for topography and with a current density cutoff equal to 0.002%. Figure 10 shows the observed versus recovered data.

We evaluate our results with the water table depth, neutron porosity (Barrash and Clemo, 2002), and capacitive conductivity (Mwenifumbo et al., 2009) taken from borehole measurements. For our borehole analysis, we choose to use the full domain of our solution. We do this because, as explained next, we are still able to extract meaningful physical information of the subsurface and, as noted in the synthetic example, our cutoff criteria can be overly conservative. The water table depth was 1 m and was measured

the same day the survey was done. Figure 9 shows that our recovered conductivity accurately images the water table boundary. We further note that the higher conductivity, sand-filled paleochannel that deepens toward the river is accurately represented.

Figure 11 shows the normalized porosity and recovered conductivity along the entire computational domain. Qualitatively, our recovered conductivity and measured porosity follow the same lowfrequency trend. This trend is mostly appreciated in Figure 11a for borehole B5, where the peak-trough-peak shape of the porosity is closely followed by the recovered conductivity beyond our solution appraisal cutoff.

Quantitatively, we compare our inversion results following Oldenborger et al. (2007a) who perform a time-lapse borehole ER monitoring of the same site in the summer of 2004. Their analysis uses Archie's law (Archie et al., 1942) to compare the formation

factor derived by ER recovered conductivity and the formation factor derived by the neutron porosity. For each borehole B5, A1, and B2, we compute the formation factor with our recovered conductivity,

$$F_{\rm ER} = \frac{\sigma_f}{\mathbf{\sigma}_z},\tag{34}$$

where σ_z denotes our recovered conductivity along the borehole and σ_f is the fluid conductivity. We take $\sigma_f = 20$ mS/m as given by Oldenborger et al. (2007a). We then invert in depth for the cementation factor m using the neutron porosity ϕ and the porosity derived from $F_{\rm FR}$,

$$\phi_{\rm ER} = \left(\frac{1}{F_{\rm ER}}\right)^{1/m}.\tag{35}$$

This gives us a depth profile for m. Using m, we compute the formation factor from the neutron porosity as

$$F_{\phi} = \frac{1}{\phi^m}.\tag{36}$$

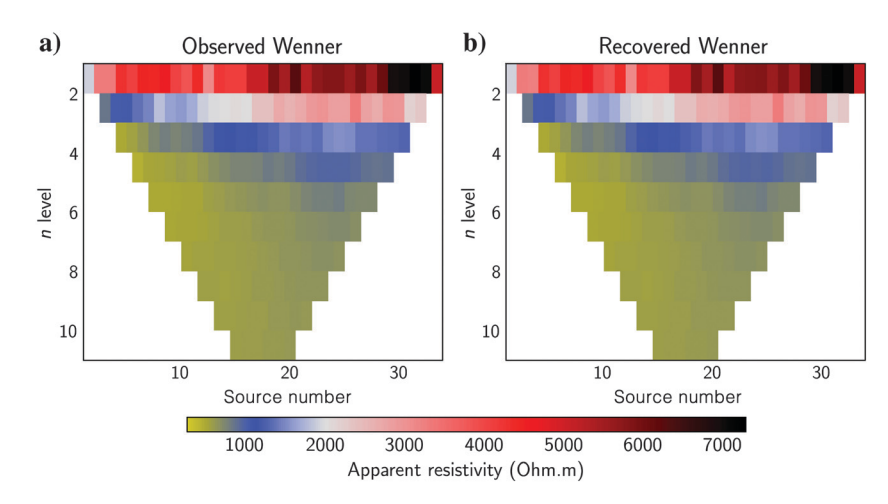


Figure 8. Wenner pseudosection of the BHRS.

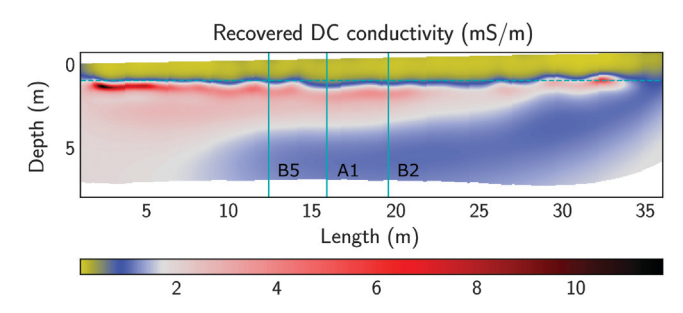


Figure 9. Recovered conductivity from the BHRS with topographic correction. The river is located toward the beginning of the survey line. The dashed cyan line represents the water table depth as measured on site (1 m deep). The solid cyan lines represent the borehole positions. Note the higher conductivity, sand-filled paleochannel that deepens toward the river. The pixel size is 0.05 m on each side.

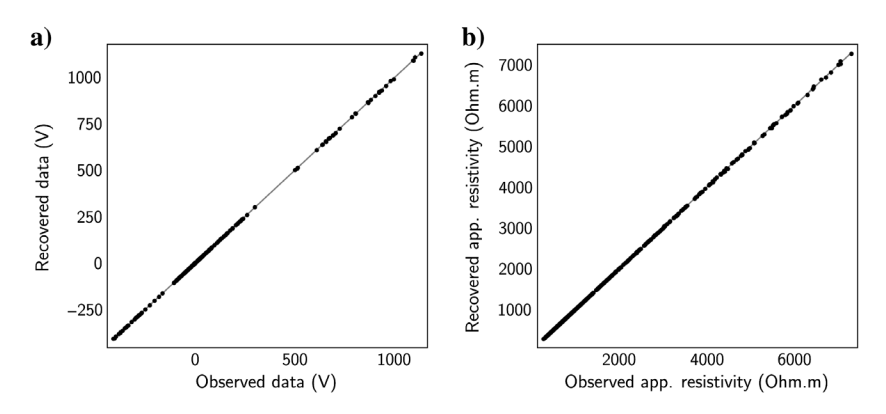


Figure 10. Observed versus recovered ER data acquired at the BHRS.

E234 Domenzain et al.

Oldenborger et al. (2007a) give average values of $F_{\rm ER}=13\pm4$, m=1.7, and $F_{\phi}=13\pm4$. In Table 3, we find similar values (within ±1 standard deviation) for $F_{\rm ER}$, F_{ϕ} , and m with our recovered conductivity.

Figure 12 shows our recovered conductivity next to the capacitive conductivity as measured by Mwenifumbo et al. (2009). Their experiment was performed in the month of November, when the river water flow had significantly decreased to a 2 m deep water table. Even though our experiments were performed with different ground water conditions, our recovered conductivity is within the same order of magnitude and follows close resemblance (to the capacitive conductivity logs) inside our appraised solution. Beyond our appraised solution near 10 m in depth, both conductivity profiles show an upward trend that is also present in the neutron porosity (Figure 11).

Finally, we compare our recovered conductivity with the result of the commercial software Res2DInv in Figure 13. Although the purpose of Res2DInv is not to recover subsurface conductivity on a very fine discretized domain, we choose to compare our results with those of this software because of its wide use in the geophysics community. Res2DInv uses a Gauss-Newton minimization scheme that stores an approximation of the Hessian at each iteration (Sasaki, 1992; Loke and Barker, 1996; Loke, 2006). The amount of memory

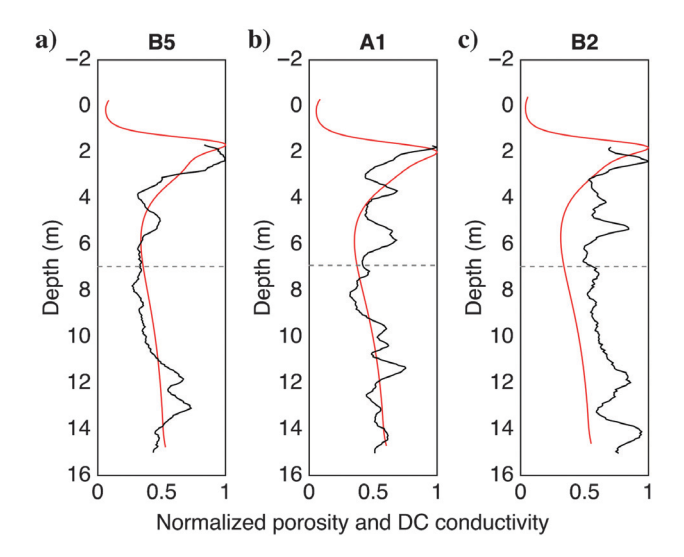


Figure 11. Normalized recovered conductivities (red) and borehole neutron porosity (black) at borehole locations in the BHRS. The dashed gray line shows the cutoff for our appraised solution.

Table 3. Formation and cementation factor appraisal for each borehole using recovered conductivity and neutron porosities.

	В5	A1	B2
m	1.8 ± 0.4	1.8 ± 0.3	1.5 ± 0.2
F_{ER}	11.9 ± 3	12.7 ± 4	13.5 ± 4
F_ϕ	14.3 ± 3	13.3 ± 4	13.4 ± 3

Our results correlate well to a previous borehole ER survey at the same site up to a standard deviation of at most ± 1 .

needed for this method is shown in dark gray in Figure 1a as a function of the domain size, and in Table 1 for different domain sizes based on relevant field data scenarios. In the Res2DInv manual (Loke, 2006), it is noted that a fine discretization can significantly increase memory requirements and is not recommended. The inversion parameters for the Res2DInv result were taken equal to those of our inversion: minimizing the L2 norm and a reference conductivity model of 2 mS/m weighed by a regularization parameter of 0.001. The horizontal grid size for the Res2DInv result was chosen as the minimum possible value allowed by the software, which is half the receiver spacing (in this case, 0.5 m). The vertical grid spacing was chosen to be 0.25 m, and the entire computational domain was set to the full rectangular xz-plane.

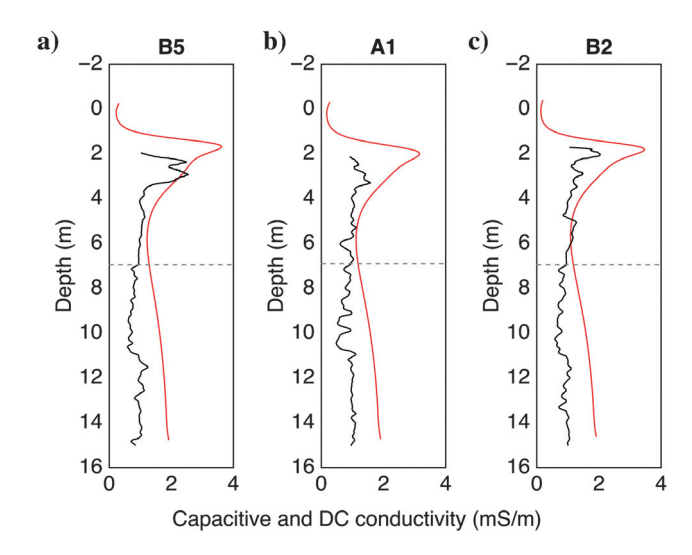


Figure 12. Recovered ER (with our method — in red) and capacitive conductivities (black) at borehole locations in the BHRS. The dashed gray line shows the cutoff for our appraised solution. Below the cutoff, the solution returns to the reference model.

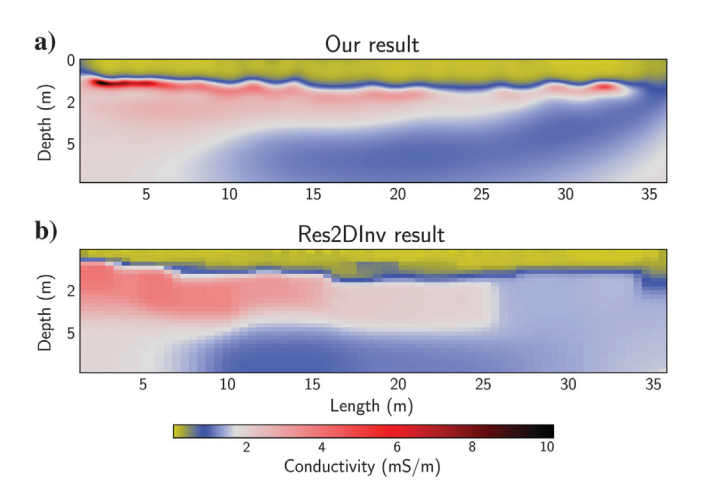


Figure 13. Comparison of (a) our result and (b) the result of the commercial Res2DInv software. The results are shown in the computational domain without applying a topographic correction. The grid size for (a) is 0.05 m in width and length, whereas for (b) it is 0.5 m long × 0.25 m wide. The smallest possible horizontal spacing in Res2DInv is half of the receiver spacing (in this case, 0.5 m).

We note that both results in Figure 13 follow the same low spatial-frequency trend: the water table is placed at approximately the same depth, and the sand channel exhibits a similar shape. However, the scheme used by Res2DInv fails to comply with time-domain finely discretized domains.

CONCLUSION

We have developed an efficient discrete adjoint-based method for inverting 2.5D ER data. We directly obtain the sensitivity of the data in the entire domain, and we do not need to approximate the Jacobian of the data using finite differences. Moreover, we take into account dissipating boundary conditions in the subsurface and do not need to store large dense matrices (such as the Jacobian of the data and the Hessian of the objective function). In geologic scenarios in which a 2.5D subsurface holds true, our algorithm linearly outperforms memory requirements for 3D gradient-descent adjoint methods. Compared with computing the 2D Jacobian of the data, our 2.5D algorithm is also linearly less memory intensive. Moreover, compared with storing a 2D Hessian matrix, our algorithm uses exponentially less memory. Regarding the operation count, our algorithm linearly outperforms 3D Gauss-Newton conjugate-gradient schemes by a factor equal to the cubed width of the 3D domain. This enables us to very finely discretize the subsurface with feasible memory requirements and a modest operation count. As a result, our algorithm can be used for joint inversion with data whose forward models impose finer grid constraints (e.g., GPR) without the need to interpolate the model parameters.

Regarding field-relevant applications that aim to join time-domain methods, our algorithm provides a memory gain of four orders of magnitude over the cheapest 3D inversion method (which is the 3D extension of the method presented here) and only a linear increase in memory over the cheapest 2D inversion method. Looking ahead as greater 3D computational capabilities become ever more possible, our algorithm can still provide an efficient alternative for 2.5D solutions.

The practical utility of our work lies in improving the efficiency and resolution of ER methods in application of joint inversions with 2.5D FWI-GPR and other geophysical data. It is a good stand-alone inversion tool in settings in which the 2.5D approximation for real earth geology is valid.

To assess the quality of the recovered parameters, we use a measure of the electric current density present in our domain throughout the iterations. This method for quality assessment takes into account the physics of the ER survey, the data, and the model parameters throughout the iterations, and it does not require extra inversions with different initial models. At worst, our method is conservative in assessing the quality of the recovered parameters. However, it is less accurate than other existing methods that explore the model space in a more exhaustive way.

We tested our algorithm on a synthetic example and on field data acquired at an alluvial aquifer near Boise, Idaho, USA. Our inversions were done on a finely discretized grid in which each square pixel had 0.05 m in side length. These discretization values comply with numerical stability requirements for GPR 2D FWI on the same field site and common geologic scenarios. Moreover, the field data inversion was performed on a domain of size relevant for GPR exploration of the subsurface (15 m deep and 45 m in length). Such a fine discretization is not supported in widely used commercially available software. This enables our algorithm to directly join the ER sensitivity of the subsurface with GPR sensitivities without the need to interpolate the domain. We find good correlation of our field data results with neutron porosity and capacitive conductivity borehole measurements taken on the site in previous surveys.

DATA AND MATERIALS AVAILABILITY

Data associated with this research are available and can be obtained by contacting the corresponding author.

APPENDIX A

FOURIER COEFFICIENTS FOR THE 2.5D TRANSFORM

To solve equation 18, we must find weights **k** and ω to accurately approximate the integral in equation 15. We follow Pidlisecky and Knight (2008) and note that the Green's function solution for homogeneous σ of equation 13 on the half xz-plane is

$$\varphi(x, y = 0, z) = \frac{i}{2\pi\sigma} \left(\underbrace{\frac{1}{\|x - s_+\|_2} - \underbrace{\frac{1}{\|x - s_-\|_2}}_{r_-}}_{1/R} \right). \quad (A-1)$$

We apply the forward Fourier-cosine transform,

$$\tilde{\varphi} = \int_0^\infty \varphi \cos(yk_y) dy = \frac{\mathbf{i}}{2\pi\sigma} (B_o(k_y r_+) - B_o(k_y r_-)),$$
(A-2)

where B_o is the zero-order modified Bessel function of the second kind. By plugging equations A-1 and A-2 into equation 18, we discretize by

ER 2.5D k and ω computation

- 1. initial guess for $\mathbf{k} = (n_k \text{ real numbers}) \cdot \Delta x$,
- 2. build $\mathbf{K}(\mathbf{k}, \mathbf{s})$,
- 3. $f \leftarrow \mathbf{K} (\mathbf{K}^{\top} \mathbf{K})^{-1} \mathbf{K}^{\top} \cdot \mathbf{1}$,
- 4. compute $\mathbf{J} = \nabla_k \mathbf{f}$ using n_k finite differences,
- 5. $\nabla_k \Phi^{\top} \leftarrow \mathbf{J}^{\top} (\mathbf{1} \mathbf{f}) + \beta \mathbf{k}$ for a fixed real number β ,
- 6. $\Delta \mathbf{k} = (\mathbf{J}^{\top} \mathbf{J} + \beta \mathbf{I})^{-1} \cdot \nabla_k \Phi^{\top}$,
- 7. $\mathbf{k} \leftarrow \mathbf{k} + \alpha \Delta \mathbf{k}$ for a fixed real number α ,
- 8. build K(k,s)
- 9. check if f is almost 1,
- 10. repeat 3-9,
- 11. $\boldsymbol{\omega} = (\mathbf{K}^{\top} \mathbf{K})^{-1} \mathbf{K}^{\top} \cdot \mathbf{1}$
- 12. return k and $\frac{2}{\pi}\omega$.

Figure A-1. Algorithm for finding the 2.5D transformation weights ω .

$$1 \approx \sum_{j} \underbrace{\frac{2R}{\pi} \left\{ B_{o}(k_{j}r_{+}) - B_{o}(k_{j}r_{-}) \right\}}_{K_{ij}} \omega_{j},$$

$$\mathbf{K} = \frac{2R}{\pi} \left\{ B_{o}(\mathbf{k}r_{+}) - B_{o}(\mathbf{k}r_{-}) \right\},$$

$$\mathbf{f} \approx \mathbf{K} \boldsymbol{\omega},$$
(A-3)

where $\mathbf{K} = \mathbf{K}(\mathbf{k}, \mathbf{s})$ is a matrix of size $n_R \times n_k$, n_R and n_k are the size of R and k, respectively, f is a vector of length n_R whose entries should approximate 1, and $\mathbf{k} = (k_{vi}), \boldsymbol{\omega} = (\omega_i)$ are vectors of length n_k . We minimize

$$\Phi(\mathbf{k}) = \|1 - \underbrace{\mathbf{K}(\mathbf{K}^{\mathsf{T}}\mathbf{K})^{-1}\mathbf{K}^{\mathsf{T}}}_{\mathbf{g}}\|_{2}^{2} = \|\mathbf{1} - \mathbf{f}(\mathbf{k})\|_{2}^{2} \qquad (A-4)$$

using a regularized Newton method. The vector of all ones is denoted as 1. Note that k and ω are geometry-dependent and not parameter-dependent. Finally, we follow Pidlisecky and Knight (2008) and use a small number for n_k , usually $n_k = 4$. Figure A-1 provides the full optimization algorithm (Pidlisecky and Knight, 2008) for computing **k** and ω .

ACKNOWLEDGMENT

This work was supported by grants DMS-1418714 and DMS-1720472 given by the National Science Foundation.

REFERENCES

- Archie, G. E., 1942, The electrical resistivity log as an aid in determining some reservoir characteristics: Transactions of the AIME, 146, 54–62,
- Barrash, W., and T. Clemo, 2002, Hierarchical geostatistics and multifacies systems: Boise hydrogeophysical research site, Boise, Idaho: Water Resources Research, **38**, 14-1–14-18, doi: 10.1029/2002WR001436.
- Barrash, W., T. Clemo, and M. D. Knoll, 1999, Boise hydrogeophysical research site (BHRS): Objectives, design, initial geostatistical results: Symposium on the Application of Geophysics to Engineering and Environmental Problems, 389–398.

 Readford J. H. W. P. Clement, and W. Parrach, 2000, Estimated.
- Bradford, J. H., W. P. Clement, and W. Barrash, 2009, Estimating porosity with ground-penetrating radar reflection tomography: A controlled 3-D experiment at the Boise hydrogeophysical research site: Water Resources Research, 45, W00D26, doi: 10.1029/2008WR006960.
- Brossier, R., S. Operto, and J. Virieux, 2009, Seismic imaging of complex onshore structures by 2D elastic frequency-domain full-waveform inversion: Geophysics, **74**, no. 6, WCC105–WCC118, doi: 10.1190/1
- Courant, R., K. Friedrichs, and H. Lewy, 1967, On the partial difference equations of mathematical physics: IBM Journal of Research and Development, 11, 215–234, doi: 10.1147/rd.112.0215.
- Dey, A., and H. Morrison, 1979, Resistivity modelling for arbitrarily shaped two-dimensional structures: Geophysical Prospecting, 27, 106–136, doi: 10.1111/j.1365-2478.1979.tb00961.x
- Doetsch, J., N. Linde, and A. Binley, 2010, Structural joint inversion of timelapse crosshole ERT and GPR traveltime data: Geophysical Research Letters, 37, L24404, doi: 10.1029/2010GL045482
- Domenzain, D., J. Bradford, and J. Mead, 2020a, Joint inversion of fullwaveform GPR and ER data — Part 1: Geophysics, **85**, no. 6, H97–H113, doi: 10.1190/geo2019-0754.1.
- Domenzain, D., J. Bradford, and J. Mead, 2020b, Joint inversion of fullwaveform GPR and ER data — Part 2: Enhancing low frequencies with the envelope transform and cross-gradients: Geophyiscs, **85**, no. 6, H115–H132, doi: 10.1190/geo2019-0755.1. Ellis, R., and D. Oldenburg, 1994, The pole-pole 3D DC-resistivity
- inverse problem: A conjugate gradient approach: Geophysical Journal International, **119**, 187–194, doi: 10.1111/j.1365-246X.1994.tb00921.x.

- Ernst, J. R., A. G. Green, H. Maurer, and K. Holliger, 2007, Application of a new 2D time-domain full-waveform inversion scheme to crosshole radar data: Geophysics, 72, no. 5, J53-J64, doi: 10.1190/1.2761848
- Forte, E., and M. Pipan, 2017, Review of multi-offset GPR applications: Data acquisition, processing and analysis: Signal Processing, 132, 210–220, doi: 10.1016/j.sigpro.2016.04.011.

 Gallardo, L. A., and M. A. Meju, 2003, Characterization of heterogeneous content and acquisition.
- neous near-surface materials by joint 2D inversion of DC resistivity and seismic data: Geophysical Research Letters, **30**, 1658, doi: 10 .1029/2003GL017370
- Groos, L., M. Schäfer, T. Forbriger, and T. Bohlen, 2017, Application of a complete workflow for 2D elastic full-waveform inversion to recorded shallow-seismic Rayleigh waves: Geophysics, 82, no. 2, R109-R117, doi: 10.1190/geo2016-0284
- Günther, T., C. Rücker, and K. Spitzer, 2006, Three-dimensional modelling and inversion of DC resistivity data incorporating topography — 2: Inversion: Geophysical Journal International, **166**, 506–517, doi: 10.1111/j
- Ha, T., S. Pyun, and C. Shin, 2006, Efficient electric resistivity inversion using adjoint state of mixed finite-element method for Poisson's equation: Journal of Computational Physics, 214, 171–186, doi: 10.1016/j.jcp.2005
- Keskinen, J., A. Klotzsche, M. C. Looms, J. Moreau, J. van der Kruk, K. Holliger, L. Stemmerik, and L. Nielsen, 2017, Full-waveform inversion of crosshole GPR data: Implications for porosity estimation in chalk: Journal of Applied Geophysics, **140**, 102–116, doi: 10.1016/j.jappgeo.2017.01 .001.
- Kochenderfer, M. J., and T. A. Wheeler, 2019, Algorithms for optimization:
- MIT Press.
 Loke, M., 2006, RES2DINV ver. 3.55, Rapid 2D resistivity & IP inversion using the least-squares method: Software manual 139, Geotomo Software.
- Loke, M. H., and R. Barker, 1996, Rapid least-squares inversion of apparent resistivity pseudosections by a Quasi-Newton method — 1: Geophysical
- Prospecting, 44, 131–152, doi: 10.1111/j.1365-2478.1996.tb00142.x. Marescot, L., S. P. Lopes, S. Rigobert, and A. G. Green, 2008, Nonlinear inversion of geoelectric data acquired across 3D objects using a finite-element approach: Geophysics, **73**, no. 3, F121–F133, doi: 10.1190/1
- Meles, G. A., J. Van der Kruk, S. A. Greenhalgh, J. R. Ernst, H. Maurer, and A. G. Green, 2010, A new vector waveform inversion algorithm for simultaneous updating of conductivity and permittivity parameters from combination crosshole/borehole-to-surface GPR data: IEEE Transactions on Geoscience and Remote Sensing, 48, 3391-3407, doi: 10.1109/TGRS
- Mwenifumbo, C. J., W. Barrash, and M. D. Knoll, 2009, Capacitive conductivity logging and electrical stratigraphy in a high-resistivity aquifer, Boise hydrogeophysical research site: Geophysics, **74**, no. 3, E125–E133, doi: 10.1190/1.3106760
- Newman, G. A., and G. M. Hoversten, 2000, Solution strategies for two- and three dimensional electromagnetic inverse problems: Inverse Problems, **16**, 1357, doi: 10.1088/0266-5611/16/5/314. Oldenborger, G. A., M. D. Knoll, P. S. Routh, and D. J. LaBrecque, 2007a,
- Time-lapse ERT monitoring of an injection/withdrawal experiment in a shallow unconfined aquifer: Geophysics, 72, no. 4, F177–F187, doi:
- Oldenborger, G. A., P. S. Routh, and M. D. Knoll, 2007b, Model reliability for 3D electrical resistivity tomography: Application of the volume of investigation index to a time-lapse monitoring experiment: Geophysics, 72, no. 4, F167-F175, doi: 10.1190/1.2732550.
- Oldenburg, D. W., and Y. Li, 1999, Estimating depth of investigation in dc resistivity and IP surveys: Geophysics, **64**, 403–416, doi: 10.1190/1
- Pan, Y., L. Gao, and T. Bohlen, 2019, High-resolution characterization of near-surface structures by surface-wave inversions: From dispersion curve to full waveform: Surveys in Geophysics, 40, 167–195, doi: 10.1007/ s10712-019-09508-0.
- Pica, A., J. Diet, and A. Tarantola, 1990, Nonlinear inversion of seismic reflection data in a laterally invariant medium: Geophysics, 55, 284-292, doi: 10.1190/1.1442836.
- Pidlisecky, A., E. Haber, and R. Knight, 2007, RESINVM3D: A 3D resistivity inversion package: Geophysics, 72, no. 2, H1–H10, doi: 10.1190/1
- Pidlisecky, A., and R. Knight, 2008, FW2_5D: A MATLAB 2.5-D electrical resistivity modeling code: Computers & Geosciences, 34, 1645-1654, doi: 10.1016/j.cageo.2008.04.001.
- Pratt, R. G., C. Shin, and G. Hick, 1998, Gauss-Newton and full Newton methods in frequency-space seismic waveform inversion: Geophysical Journal International, **133**, 341–362, doi: 10.1046/j.1365-246X.1998
- Rumelhart, D. E., G. E. Hinton, and R. J. Williams, 1986, Learning representations by back-propagating errors: Nature, **323**, 533–536, doi: 10 1038/323533a0

- Sasaki, Y., 1992, Resolution of resistivity tomography inferred from numerical simulation 1: Geophysical Prospecting, **40**, 453–463, doi: 10.1111/j.1365-2478.1992.tb00536.x.
- J.1365-24/8.1992.tb00536.x.

 Taillandier, C., M. Noble, H. Chauris, and H. Calandra, 2009, First-arrival traveltime tomography based on the adjoint-state method: Geophysics, 74, no. 6, WCB1–WCB10, doi: 10.1190/1.3250266.

 Tripp, A., G. Hohmann, and C. Swift, 1984, Two-dimensional resistivity inversion: Geophysics, 49, 1708–1717, doi: 10.1190/1.1441578.

 Zhang, J., R. L. Mackie, and T. R. Madden, 1995, 3-D resistivity forward modeling and inversion using conjugate gradients. Geophysics, 60.
- modeling and inversion using conjugate gradients: Geophysics, **60**, 1313–1325, doi: 10.1190/1.1443868.
- Zhou, Z., A. Klotzsche, T. Hermans, F. Nguyen, J. Schmäck, P. Haruzi, H. Vereecken, and J. van der Kruk, 2020, 3D aquifer characterization of the Hermalle-Sous-Argenteau test site using crosshole GPR amplitude analysis and full-waveform inversion: Geophysics, **85**, no. 6, H133–H148, doi: 10.1190/geo2020-0067.1.

Biographies and photographs of the authors are not available.